Eur. Phys. J. B **19**, 87–95 (2001)

THE EUROPEAN PHYSICAL JOURNAL B

EDP Sciences

Two dimensional hydrothermal waves in an extended cylindrical vessel

N. Garnier[a] and A. Chiffaudel[b]

SPEC, CEA Saclay, Orme des merisiers, 91191 Gif-sur-Yvette Cedex, France

Received 12 May 2000 and Received in final form 26 October 2000

Abstract. We report experimental results for hydrothermal waves instability in thermocapillary-driven flow in an extended cylindrical geometry. The waves are shown to appear *via* a supercritical I_o instability. At larger fluid depth, the conventional predictions of Smith and Davis – planar waves referred to as HW1 – are observed. For smaller depth, *i.e.* for larger aspect ratios, a new kind of spatial behavior is reported which may be interpreted as a new instability. This new instability is localized in the center of the cell and its spatial structure close to onset resembles targets, *i.e.* purely radial waves. We refer to these hydrothermal waves as HW2.

PACS. 47.54.+r Pattern selection; pattern formation – 47.20.-k Hydrodynamic stability – 47.27.Te Convection and heat transfer – 47.35.+i Hydrodynamic waves

1 Introduction

Thermocapillary convection occurs in many different engineering situations such as surface coating or liquid bridges in directional solidification for example [1]. In all those systems, the variation of the surface tension with the temperature leads to the Marangoni effect in which a temperature gradient drives a thermocapillary convective flow. Such flows were shown to be subject to the so called hydrothermal wave instability by Smith and Davis [2]. Many experimental [3–6], theoretical and numerical [2,4,7,8] studies were devoted to the hydrothermal waves in different geometries. Here we focus on the spatial properties of the waves in the case of the bidimensionally extended system obtained when the vertical dimension is very small compared to the two horizontal ones, and of the order of the capillary length.

The thin horizontal fluid layer is subject to an imposed horizontal temperature gradient which drives a basic flow, in which the velocity of the fluid is finite everywhere and proportional to the temperature gradient.

When the temperature gradient is increased, a pattern forming instability occurs, in the form of traveling waves. The theoretical linear stability analysis was performed in an infinite system in the absence of gravity forces by Smith and Davis [2] who discovered the hydrothermal waves instability. This study was then completed by Mercier and Normand [7] who considered the additional effect of buoyancy and Priede and Gerbeth [8] who examined the convective nature of the instability at onset. Let us point out that below the wave instability threshold, the basic flow may break up into standing co-rotating rolls if the depth of the layer is large enough [6,9]. Moreover, if we denote the wavevector in the horizontal plane $\mathbf{k}$ and define the propagation angle ψ as the angle between the horizontal temperature gradient $\boldsymbol{\nabla} T$ and this wavevector, it was shown that hydrothermal waves are planar waves which propagate with $\mathbf{k} \cdot \boldsymbol{\nabla} T > 0$, *i.e.*, from the cold side towards the hot side, with an angle of propagation depending on the Prandtl number Pr [2]. For small Pr, $\mathbf{k}$ is almost parallel to $\boldsymbol{\nabla} T$ whereas for large Pr, it is almost perpendicular to $\boldsymbol{\nabla} T$.

Many experiments have been performed with horizontal temperature gradients in simple different extended geometries. Low Prandtl number fluids (liquid metals) were not studied because of the difficulty to maintain a clean free surface. Very high Prandtl number fluids such as high viscosity silicon oils did not reveal any time-dependent instability. So experiments in which this instability occurred were all performed with intermediate Pr, such as acetone, alcohol or low viscosity silicon oil (this paper). For such medium Prandtl numbers (4–20), an intermediate angle of propagation is expected.

The first direct observation of hydrothermal waves was performed in a long rectangular channel extended only in the direction perpendicular to the temperature gradient by Daviaud and Vince [3]; they saw waves with a propagation angle of 80° corresponding to propagation along the channel. A similar behavior was reported in a long annular channel [10]. On the contrary, Platten *et al.* [4] used a rectangular cell confined in the horizontal direction perpendicular to the temperature gradient in which the waves were forced to propagate along the gradient.

[a] e-mail: garnier@spec.saclay.cea.fr
[b] Centre National de la Recherche Scientifique

Those experiments were confined in a direction and so the angle of propagation was constrained. When increasing the dimensions in both horizontal directions, a finite constant propagation angle was observed, for example in silicon oil by Riley and Neitzel [5], Pelacho *et al.* [6]. In all those experiments, the waves travel from cold to hot side with a constant angle of propagation. We will refer to these planar hydrothermal waves as HW1 [11]. Burguete *et al.* [12] looked at the effects of both the confinement in the gradient direction and the fluid depth; they showed that for small depth and/or large extent between the hot and the cold side, the source of hydrothermal waves could be located in a point region and emit cylindrical waves, *i.e.*, waves with a varying propagation angle.

A cylindrical geometry was studied by Schwabe *et al.* [13], in an extended cylindrical cell heated from the center; in this case, the authors found an oscillatory instability but did not report the spatial pattern in 2D.

The present work will show experimental evidence for a localized wave instability in which the angle of propagation varies with the applied temperature gradient; we will call these waves HW2. We report here an experiment in a large cylindrical cell heated from the outside and cooled from the center with a thin fluid layer. The waves we observe propagate from the cold center to the hot external boundary of the cell. For small fluid depth, waves are emitted by a point source – the center of the cell – with a purely radial wavevector at onset, which make them look like targets [14]. The pattern remains localized around this source.

This paper is organized as follows: we first describe the experimental apparatus in Section 2 and report the quantitative observations and characteristics of HW2 in Section 3. A brief qualitative report of HW1 is given in Section 4. Direct temperature measurements are presented and commented in Section 5. Discussion and conclusion then close the paper in Section 6.

2 Apparatus

2.1 Convection cell

We impose a radial temperature gradient by the thermalization of 2 copper blocks with circulating water, see Figure 1. The inner block is a cylinder of diameter $d_{\rm int} = 8$ mm, with temperature denoted $T_{\rm int}$. The outer block is a cylinder of internal diameter $d_{\rm ext} = 135$ mm with temperature $T_{\rm ext} > T_{\rm int}$. The temperature measurements are performed using platinum thermoresistances located in the copper blocks, 1 millimeter close to the fluid boundary. In our experiment, the control parameter is the temperature difference $\Delta T = T_{\rm ext} - T_{\rm int}$, indicating the distance from the thermal equilibrium state, and ranging from 0 to 20 K, with a precision of typically ± 0.02 K.

The bottom of the cell is made of a plane glass mirror of thermal conductivity $\kappa_{\rm m}$ filling the gap between the two blocks. The operating fluid is silicon oil V065 (polysiloxane) from Rhodia, with viscosity $\nu = 0.65 \times 10^{-6}$ m^2 s^{-1}, Prandtl number $Pr = 10$ and thermal conductivity $\kappa_{\rm f}$.

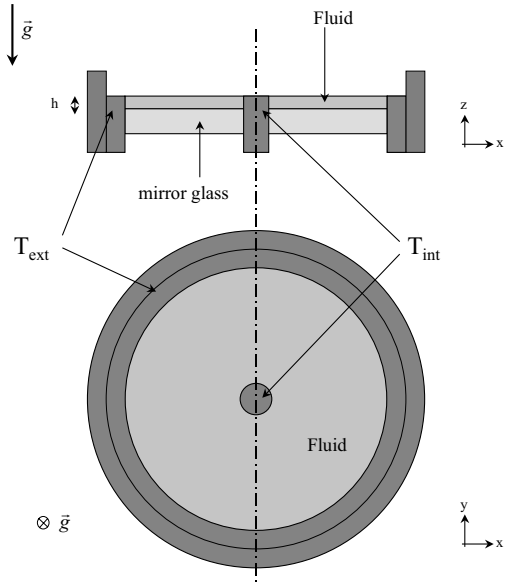

Fig. 1. Sketch of the apparatus and the geometry. $\Delta T = T_{\rm ext} - T_{\rm int} > 0$ in all the experiments.

The upper surface of the fluid is its interface with gas (air and oil vapor) of conductivity $\kappa_{\rm a}$. The thermal boundary conditions are such that: $\kappa_{\rm a} \ll \kappa_{\rm f} \ll \kappa_{\rm m}$, *i.e.*, the bottom is conducting and the top surface is insulating.

The depth of the layer can be varied but the main results reported here were obtained with $h = 1.2 \pm 0.05$ mm. Thus the two horizontal aspect ratios $\Gamma_r = (d_{\rm ext} - d_{\rm int})/2h = 55.2$ and $\Gamma_\theta = \pi(d_{\rm ext} + d_{\rm int})/2h = 187.2$ are constant and large enough to consider our system as "two-dimensional", by opposition to the case of one-dimensional systems [3,10] in which the traveling waves are forced to propagate in a single direction, and all the information on the spatial structure is therefore contained in one spatial dimension. Some of our experiments were performed with $h = 1.9$ mm – close to the depth used in [3,10] – thus giving $\Gamma_r = 33.4$ and $\Gamma_\theta = 118.2$, still two-dimensional. The observations are qualitatively different and are briefly exposed in Section 4; quantitative results will be reported elsewhere.

In order to avoid menisci up on the lateral boundaries, we have made the top of those copper boundaries being always located 0.05 mm below the free surface. This approach is almost the same as the one used in references [5,13], but it allows some little deviations from the average fluid depth. So there is a 0.05 mm layer covering the two copper blocks. This layer is at rest: its Rayleigh and Marangoni numbers, measuring the buoyancy ability, are very small even for greater values of $T_{\rm ext}$, and so always lower than the critical values leading to Bénard-Marangoni convection.

The silicon oil we use is volatile and we keep the right level of fluid by injecting oil with a regulation apparatus. The fluid level changes are optically monitored: a light beam is sent on the surface with an incidence angle of 45°, most of it enters the fluid and is reflected by the bottom mirror before exiting the fluid and being received

by a two-quadrants photodiode. Each quadrant of this device produces an electrical potential difference proportional to the light intensity it receives. Changes in fluid depth causes changes in the optical path and results in a displacement of the impact points of the beam over the photodiode quadrants. The induced differential electrical signal then reflects a fluid depth smaller or larger than the reference value and we use this information to move up or down a tank to inject or remove fluid from the convection cell. This regulation loop allows us to operate at different values of $T_{\rm ext}$ and $T_{\rm int}$, *i.e.*, at different values of the evaporation rate, with a constant fluid depth for long experience times. The latest experiments have also been performed with the cell closed with a glass window (for visualization) located several centimeters above the free surface, which reduces both evaporation and the noise due to gas circulation but does not change any quantitative result.

2.2 Measurement techniques

The perfect transparency of the silicon oil allows us to use shadowgraphy to make both qualitative and quantitative observations. A CCD camera with 256 gray levels and a computer are used to digitalize the signal; we make both snapshots and spatio-temporal diagrams of simple geometrical loci; we use circles and radii, both centered with the cell to obtain information about two perpendicular directions, in order to completely describe the wave number components: we have access to its projections along radial and azimuthal direction. Examples of photographs are given in Figure 2. All amplitude, wavenumber and frequency data are obtained by Hilbert transforms over the spatio-temporal diagrams.

A thin thermocouple (Alumine/Chromel) is also used to record the radial temperature dependence of the basic state at different depths. Those measurements are presented in Section 5.

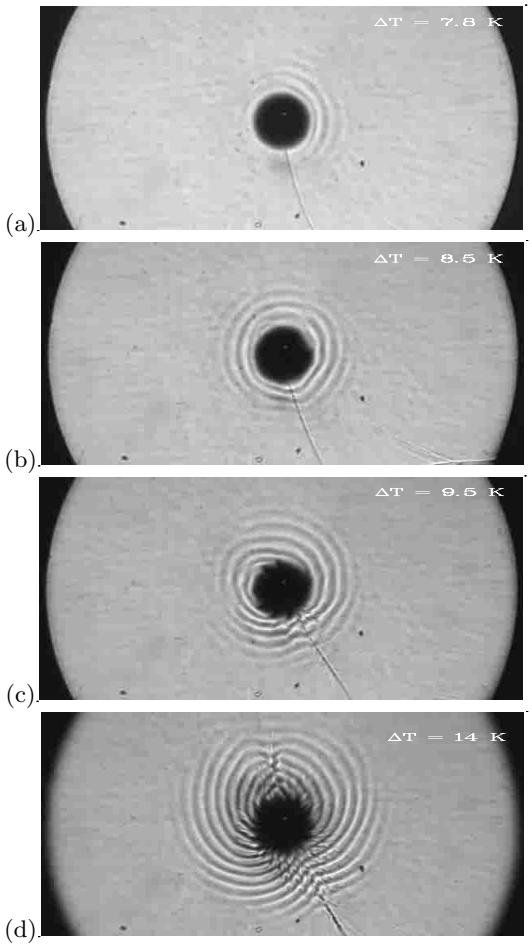

Fig. 2. Shadowgraphy snapshots of the cell for $h = 1.2$ mm. (a) $\Delta T = 7.8$ K: slightly above onset, purely radial time-dependent target pattern. (b) $\Delta T = 8.5$ K: azimuthal symmetry is slightly broken. (c) $\Delta T = 9.5$ K and (d) $\Delta T = 14$ K: the pattern looks like spirals, with left-turning and right-turning waves regions separated by sources and sinks. The thin radial line at the bottom of each photograph is a defect of the basic flow.

3 Results: critical behavior of HW2 instability

3.1 Characterization of the first instability: amplitude and frequency

For $0 \leq \Delta T < \Delta T_{\rm HW2} = 7.6 \pm 0.1$ K, neither oscillating nor time-dependent flow is observed; this is what we call the basic state. This flow corresponds to a flat torus [15]. No co-rotating rolls modulations of this torus are observed [6]. The regularity of the basic flow is easily broken by external perturbations such as air movements, and radial defects are often observed (Fig. 2).

For $\Delta T > \Delta T_{\rm HW2}$, in addition to the basic state, a wave pattern is present in the cell, localized near the cold center. Owing to their 2D spatial behavior (see below), these hydrothermal waves are labeled HW2. Close to the onset, the wave pattern looks like pulsing targets and the copper block at the center of the cell behaves like a source of radial waves. For higher ΔT, the pattern looses its azimuthal symmetry. Examples of such a pattern are seen in Figure 2. We look at the local amplitude of the wave pattern, given by the shadowgraphic technique and complex demodulation, to determine the value of the threshold $\Delta T_{\rm HW2}$.

This local amplitude, averaged on a radius, is proportional to $(\Delta T - \Delta T_{\rm HW2})^{1/2}$, as seen in Figure 3. At this value, the transition to the wave-state is analogous to a second order phase transition: it is the result of a supercritical instability. This behavior is illustrated in Figure 3, showing the 1/2 critical exponent for the order parameter dependence on ΔT near the transition point. Owing to the cylindrical geometry, the radial average represents a global measure of the wave amplitude over the entire cell.

Moreover, the instability is oscillatory, *i.e.*, with a non vanishing frequency as can be seen in Figure 3, where the frequency is plotted *versus* ΔT. The plotted value of the frequency is obtained by averaging the local frequency over a circle; it is almost constant whatever the

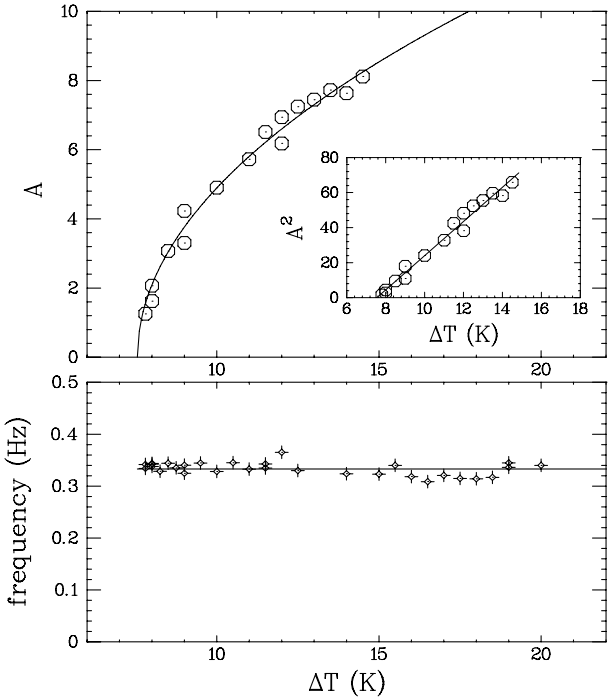

Fig. 3. Top: Local amplitude of the wave pattern averaged on a single radius *versus* ΔT; circled points stands for experimental results and solid curve is the square root fit. Bottom: Frequency of the waves at $r = 16.4$ mm from the center *versus* ΔT.

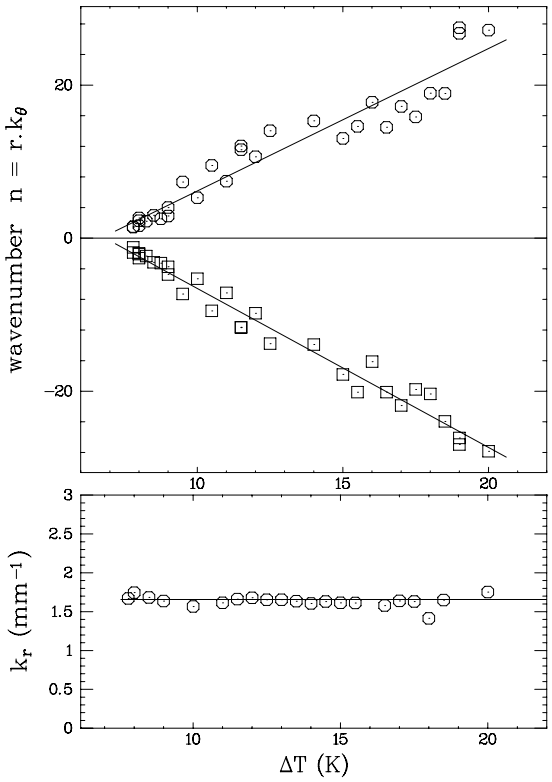

Fig. 4. Wavevector components of the HW2 waves at distance $r = 16.4$ mm from the center *versus* the temperature difference ΔT. Upper part of the figure: azimuthal wavenumber $n = rk_\theta$, positive for right-turning waves and negative for left-turning waves. Lower part of the figure: radial wavenumber k_r. For a given ΔT, those values n and k_r are almost uniform in the cell.

temperature difference is, and varies very little with the position in the cell; see also Figure 13. As we will see in the next section, the wavenumber is finite at onset, thus the HW2 instability is a $\mathrm{I_o}$ instability [16].

3.2 Wave vectors and spatial behaviors

Even more interesting are the properties of the wavevector which in our 2D cylindrical geometry is described with two cylindrical coordinates $k_r = \mathbf{k} \cdot \mathbf{e}_r$ and $k_\theta = \mathbf{k} \cdot \mathbf{e}_\theta = n/r$, where r is the local radius and n is the number of wavelengths in the azimuthal direction. As we can see, there is no relation between k_r and k_θ which behave independently with ΔT (Fig. 4). This justify the "2D" labeling of this hydrothermal waves instability (HW2) by opposition to the unidimensional hydrothermal waves (HW1) predicted by linear stability theory [2]. These waves, previously seen in [5,6,12] and reported here in Section 4, are characterized by the proportionality between k_r and k_θ. The knowledge of k_r and k_θ allows the computation of the angle $\psi = (\mathbf{e}_r, \mathbf{k})$ between the temperature gradient and the wavevector. We have:

$$\psi = \arctan\left(\frac{k_\theta}{k_r}\right) = \arctan\left(\frac{n}{rk_r}\right).$$

The variation of ψ *versus* ΔT at a fixed position in the cell is represented in Figure 5.

A main result of our study is the linear vanishing of k_θ with $(\Delta T - \Delta T_{\mathrm{HW2}})$ (Fig. 4), *i.e.*, the fact that we can

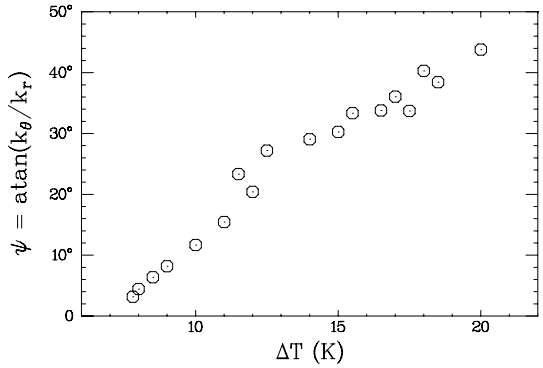

Fig. 5. Angle of propagation ψ of HW2 at distance $r = 16.4$ mm from the center *versus* the temperature difference ΔT. ψ is defined as the angle between $\boldsymbol{\nabla} T$ and $\mathbf{k}$ and is computed using data from Figure 4.

define another order parameter, with a critical exponent of 1. This behavior of k_θ changes qualitatively the pattern structure: from a concentric – roll-like – pulsing target at onset, we then have a spiraling pattern – with more and more spiral branches – as we get higher above onset. This is illustrated in Figure 2.

Moreover, the region unstable to the 2D waves is localized near the center as can be seen in Figure 6 where

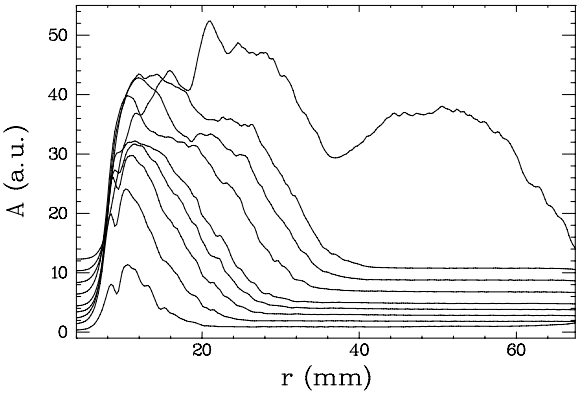

Fig. 6. Amplitude profiles along radius r for different ΔT. The fluid is located between $r = 4$ mm and 67.5 mm. For clarity, profiles are shifted in the vertical direction proportionally to ΔT. The values of ΔT are 8, 9, 10, 11, 12, 14, 16, 18 and 20 K. For this last value, HW1 are present in the outer region ($r > 35$ mm).

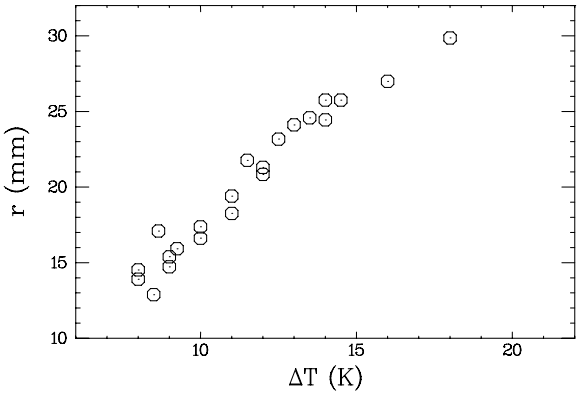

Fig. 7. Radial position of the HW2 front from the center of the cell, *versus* ΔT. The fluid is located between $r = 4$ mm and 67.5 mm.

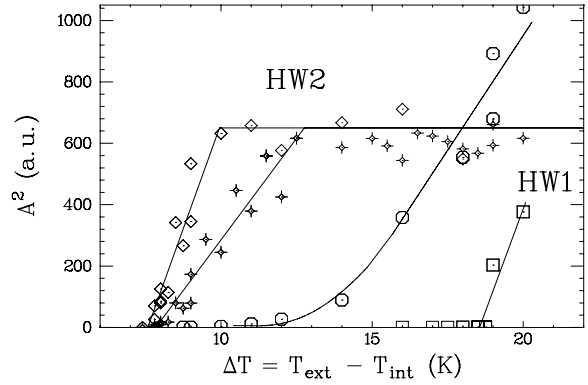

Fig. 8. Amplitude of the waves at various distance r from the center: $r = 11.7$ mm ($\diamond$), $r = 16.4$ mm ($+$), $r = 21.1$ mm ($\circ$). The $\square$ symbols, corresponding to $r = 40.3$ mm, show specifically the HW1 pattern which arises at $\Delta T = 18.5$ K (see Sect. 4). All solid lines and curves are guide for the eye.

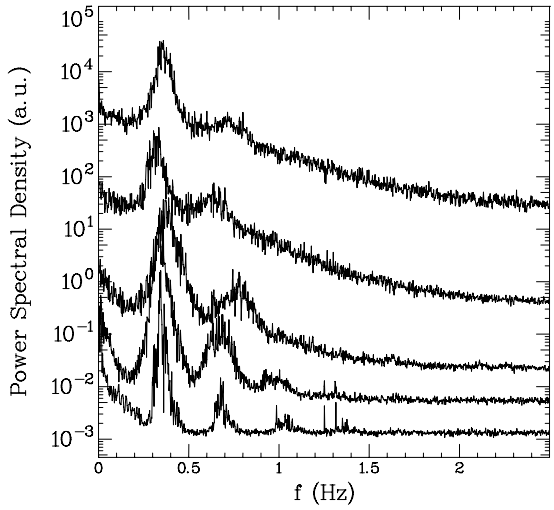

Fig. 9. Averaged power spectra, for different values of the control parameter $\Delta T = 8$, 10, 12, 16 and 20 K. For clarity, the spectra have been shifted in the vertical direction proportionally to ΔT. On the spectrum for $\Delta T = 8$ K, the main peak is narrow, so the harmonics. On the spectrum for $\Delta T = 16$ and 20 K, the peaks (main and harmonics) are wide. Beyond the first harmonic, a power law can even be extracted for the spectrum. A snapshot corresponding to the $\Delta T = 20$ K pattern is presented in Figure 12. Time spectra have been averaged along a radius.

the amplitude profile along a radius, at a fixed azimuthal position in the cell, is plotted for different values of ΔT. Increasing the temperature difference is shown to increase the region occupied by the HW2. Figure 7 shows the evolution with ΔT of the front position limiting the region where HW2 exist; this position is defined as the one for which the amplitude is half the maximum amplitude of the corresponding profile. As one can see in Figure 7, the position of the front evolves linearly with ΔT and so the pattern invades the cell.

As was pointed out in Figure 3, the average amplitude over a radius increases smoothly from ΔT_{HW2} but the local amplitude evolution depends on the radial position, as suggested by Figure 6. The critical evolution of the local amplitude averaged along circles of different radii r is represented in Figure 8. For locations near the center (diamonds and crosses in Fig. 8), the instability appears at $\Delta T_{\mathrm{HW2}} = 7.6 \pm 0.1$ K. The local amplitude behaves first with a critical exponent 1/2 and then reaches saturation. In the middle of the cell, the bifurcation is imperfect (circles in Fig. 8). For $r \gtrsim 40$ mm, the amplitude is always zero: the HW2 pattern remains localized near the center; but for larger ΔT, HW1 instability sets in as it will be commented in the next section.

As ΔT is increased, the spiraling pattern quickly reaches a chaotic state, with a wide band of allowed wavenumber and frequencies. The broadening of the spectrum can be seen in Figure 9, and is quantified in Figure 10, where the width Δf of the main peak, corresponding to the hydrothermal waves, is plotted *versus* ΔT. This is an indirect measure of the number of modes excited at a given value of the control parameter ΔT. This number increases with the temperature constraint following

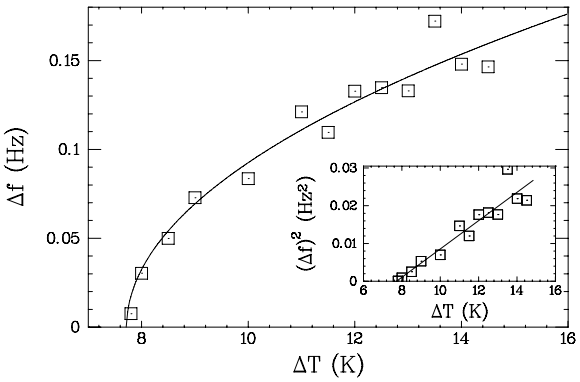

Fig. 10. Width of the peak corresponding to HW2 in spectra, *versus* ΔT; the spectra have been averaged along a radius.

a square-root behavior: $\Delta f \propto (\Delta T - \Delta T_{\rm HW2})^{1/2}$. These data can be used to track the threshold value and we then find 7.7 ± 0.1 K, in good agreement with the amplitude data of Figure 3. Patterns corresponding to wide spectra may be due to the large spatial extension – large aspect ratios – and so the large number of degrees of freedom. Local amplitudes get saturated (Fig. 3) and so the energy, proportional to $(\Delta T - \Delta T_{\rm HW2})^{1/2}$, is distributed over a wide range of modes.

4 The classical hydrothermal wave instability: HW1

Let us briefly present the results on another hydrothermal wave instability. When studying thermocapillary instabilities in the same cell but with a different depth $h = 1.9$ mm, we have shown that a different kind of hydrothermal waves appears as a supercritical $\rm I_o$ instability [11]. Their equiphases almost fit the law $r \propto \theta$, *i.e.*, are Archimedean spirals (see Fig. 11). The angle ψ between the temperature gradient and the wavevector is almost uniform in space (varying typically from 60° to 40° along r) and independent of ΔT. So $n = k_\theta / r$ is proportional to k_r and both are independent of the temperature difference. The Archimedean spiral pattern can then be described using only one wavenumber component – k_r or n – just as in the case of an unidimensional system. So we call those waves "1D hydrothermal waves" (HW1) and we remark that the theory of Smith and Davis [2], predicting a constant angle of propagation between the gradient and the wave-vector is well verified for the HW1 if we use n as the orthoradial wavenumber, whereas it is not for the HW2. We believe that HW1 were the kind of hydrothermal waves observed in long unidimensional channels [10,11]. Please note that the constant angle between the imposed temperature gradient and the wavevector reduces the number of degrees of freedom for the description of the wave-vector from the value 2 (two free components) to the value 1 (one free component). So HW2 are waves with wave-number described by two independent spatial components (k_r, k_θ) whereas HW1 are

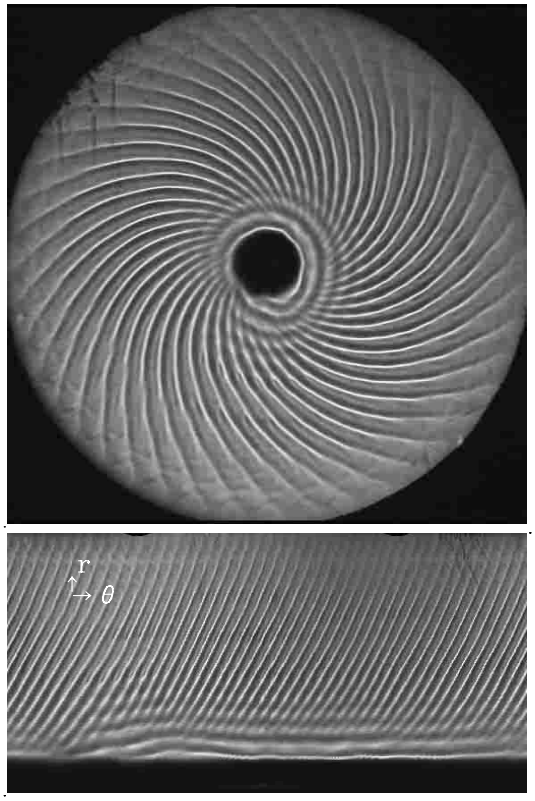

Fig. 11. Shadowgraphic photograph of the cell for a higher fluid depth $h = 1.9$ mm and $\Delta T = 14.25$ K. HW1 is observed as rotating Archimedean spirals. Please note that the circular pattern localized near the center corresponds in this case to stationary corotating rolls – a modulation of the basic thermocapillary flow [9] – that should not be mistaken for the time-dependent HW2 instability. The top picture is a direct representation, and the bottom one is a representation in the orthogonal plane (θ, r).

described by one component (k_θ), usually the component perpendicular to the temperature gradient as in references [3,10,12]. Another difference between HW1 and HW2 is the fact that the HW1 pattern is not localized near the cold end wall but invades the whole cell as soon as the onset is crossed.

Note that this HW1 instability occurs on a roll-modulated basic flow, as can be observed in Figure 11 close to the center of the cell. On the contrary, HW2 instability at smaller depth $h = 1.2$ mm occurs on a non-modulated basic flow. The existence of stationary rolls over the basic flow for larger fluid depth confirms the observations in an extended rectangular cell [6]. A detailed study of this structure in the present geometry is under progress.

Let us come back to the aim of this paper, *i.e.*, the description of the waves observed at $h = 1.2$ mm. For $\Delta T > \Delta T_{\rm HW1} = 18.5$ K, there is a qualitative change in the observed pattern which was formerly only composed by HW2. The waves now invade all the cell, and are no more localized near the center (for $\Delta T = 20$ K, see photograph in Fig. 12 and amplitude profile in Fig. 6).

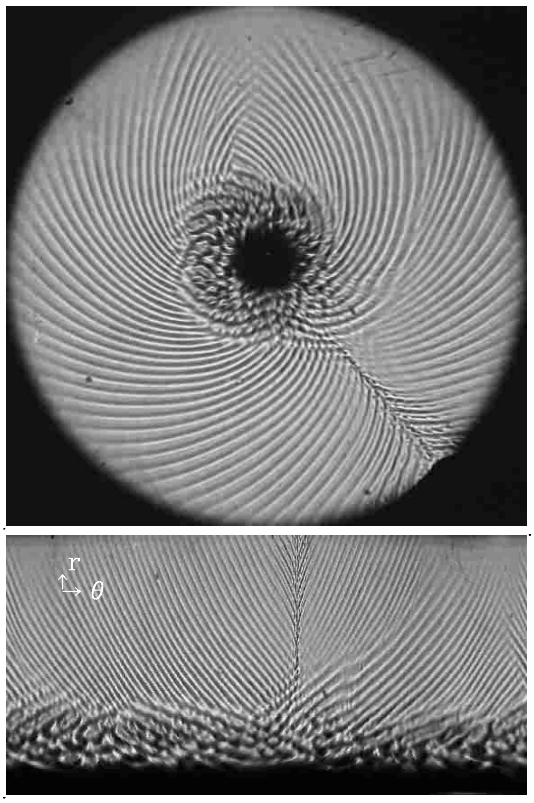

Fig. 12. Shadowgraphic photograph of the cell for $h = 1.2$ mm and $\Delta T = 20$ K. The top picture is a direct representation, and the bottom one is a representation in the orthogonal plane (θ, r).

We interpret this as a new HW1-pattern superposing over the existing HW2-pattern. HW2 remains dominant close to the center but HW1 spiral waves invades all the rest of the cell. This picture is clearer if we represent the data in the (θ, r) plane (Fig. 12); the wavelength in the region occupied by HW2 is larger than the wavelength in the region where no waves previously existed.

Let us point out that these HW1 are not a secondary instability of the former HW2 pattern. First, HW1 and HW2 exist in different locations in the cell. Second, HW2 are already subject to secondary instabilities: one can see sources and sinks, wavelengths annihilations and phase modulations below the onset of HW1. Those secondary instabilities are tracked by the broadening spectra (Fig. 9). Just as for HW2, the HW1 instability is a supercritical I_o instability (Fig. 8). The critical wavenumber and frequency of HW1 and HW2 are slightly different: Snapshot (Fig. 12) shows the difference between both wave-vectors. Figure 13 – a radial frequency profile – shows the two HW1- and HW2-domains oscillating at slightly different frequencies.

It is worth mentioning that the two wave-patterns produced by the two instabilities interact together: as HW2 is almost turbulent at the HW1 threshold, the resulting pattern behaves chaotically. HW1 are thus being forced by turbulent HW2. The quantitative study of the HW1 instability, for $h = 1.9$ mm, will be reported elsewhere.

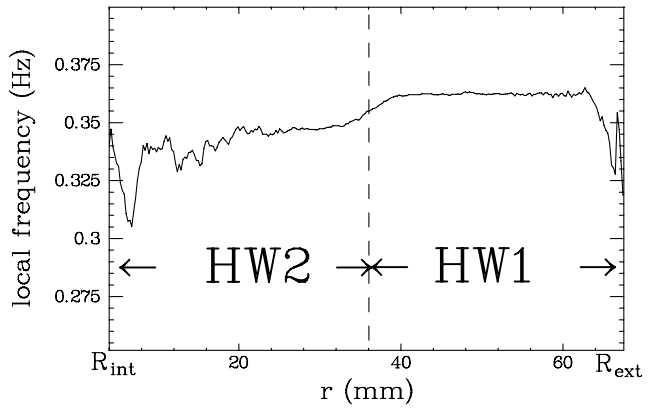

Fig. 13. Radial frequency dependence for $\Delta T = 20$ K. In the HW1 region, the frequency is constant and different from the value in the HW2 region, near the center.

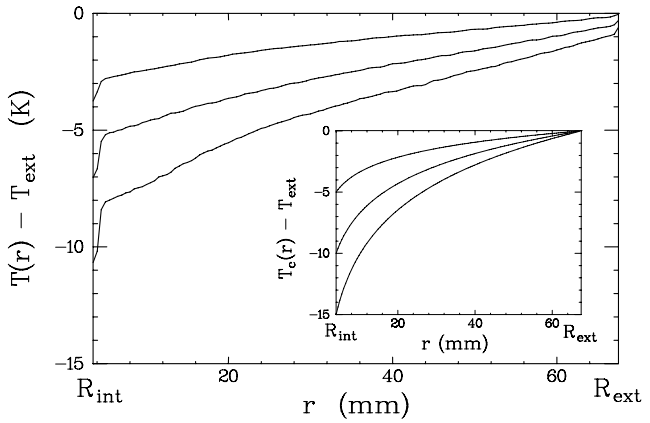

Fig. 14. Horizontal temperature profiles along a radius. The total fluid depth is $h = 1.2$ mm. Each point is the average value of the temperature measured at $z = 0.3$, 0.6, 0.9 and 1.2 mm. The three curves correspond to an imposed temperature gradient $T_{\rm ext} - T_{\rm int} = +5$, +10 and +15 K (from top to bottom). The inset gives the theoretical conductive profiles in each case.

5 Temperature profiles

The localization of HW2 instability near the center of the cell may be due to the cylindrical geometry: the conductive regime – as in the mirror bottom – is characterized by a logarithmic distribution of the temperature in the radial direction, suggesting a much stronger temperature gradient near the center. In order to test this point, we have performed temperature measurements to determine the local temperature gradient. For this, we average four temperature r-profiles (for different $z = 0.3$, 0.6, 0.9 and 1.2 mm) which are almost similar; the resulting profiles are presented in Figure 14 for $\Delta T = 5$, 10 and 15 K. The theoretical gradient should be hyperbolic in the perfectly conductive case. Experimentally however, the gradient is observed to be almost constant in the bulk of the cell, to within a few percent. We observe two boundary layers, a small one close to the outside boundary (hot) and a stronger one close to the inner rim (cold). The cold boundary layer contributes to approximately one half of the total

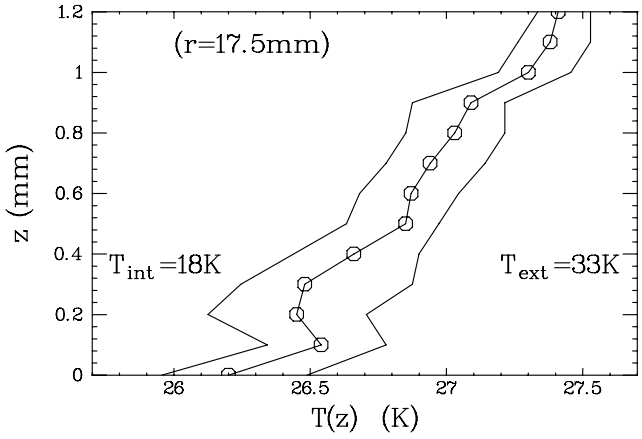

Fig. 15. Vertical temperature profiles at $r = 17.5$ mm, for $h = 1.2$ mm and $T_{\rm ext} - T_{\rm int} = 33 - 18 = 15$ K. The center curve – circles – corresponds to the averaged data and the two lateral ones correspond to the extreme values. See text for details.

temperature difference. Due to the specific imposition of the temperature gradient over the cell (the copper blocks are totally immersed), there is a vertical temperature gradient between the free liquid surface and the air. This implies the existence of a heat flux at the surface which depends strongly on the coordinate r. This explains the asymmetry between both boundary layers and the departure from the conductive logarithmic temperature profile. The evaporation due to the oil volatility also contributes to a vertical temperature gradient and therefore also distorts the horizontal temperature profile. The characteristic size of the boundary layer is very small (less than 1 mm) and cannot explain the localization of the HW2 pattern, which is several wavelengths long in the radial direction at threshold (typically 10 mm). Far from this boundary layer, the temperature gradient is uniform, as in the rectangular case, and so the classical theory of Smith and Davis for hydrothermal waves should be applicable.

Figure 15 shows the vertical temperature dependence for $r = 17.5$ mm and $\Delta T = 15$ K, in the wave-existence zone. The temperature signature of the hydrothermal waves is an oscillation of temperature in the region where waves exists, and so extreme values are plotted. The amplitude of the oscillation is slightly greater close to the bottom than at the free surface but globally, the wave appears to occupy the whole layer of fluid. We have checked that all temporal information given by shadowgraphy is exactly the same as those given temperature measurements, just as in references [6,12].

6 Summary and discussion

We have investigated the behavior of a non-linear wave instability in an extended geometry, and observed two different patterns issuing from two different instabilities, labeled HW1 and HW2. HW1 propagate as predicted by linear stability analysis [2,8] in that the two components of the wave vector are proportional and define a constant angle $\psi = (\mathbf{e}_r, \mathbf{k})$ between the temperature gradient and the wavevector. This angle is almost constant in the cell and depends probably on the Prandtl number [2]. HW1 are the only hydrothermal waves obtained in cells with the smaller aspect ratio Γ_r in the direction of the temperature gradient [3,10–12]. But they can exist for larger values of this aspect ratio and have been observed in extended rectangular geometry [6] and here in cylindrical geometry. If the geometry is confined, as in [4], it is even hard to define this angle because the waves are then forced to propagate along the extended direction of the gradient. Here, we have isolated HW2 which are another wave system obtained only when the aspect ratio is large and the depth small. HW2 differs qualitatively from HW1 on two spatial properties:

- the angle ψ, given at constant distance from the center ($r = 11.6$ mm), varies from 0° at onset to 45° at $\Delta T = 20$ K (Fig. 5) instead of being constant and close to 60° for HW1,
- HW2 are localized wave-patterns, with a fixed front position whereas HW1 always extend everywhere in the cell once the onset is crossed.

On the quantitative point of view, both HW1 and HW2 appear through a supercritical $\mathrm{I_o}$ instability. The frequency and the modulus of the wavenumber of these structures are of the same order of magnitude whatever the fluid depth is (1.2 or 1.9 mm) and they are of the same order as the values measured with the same fluid in different geometries [3,10,12]. When both HW1 and HW2 are present (1.2 mm), we checked that the frequency and the wavevector were different in the two structures.

Note that the orientation of the temperature gradient is important because the symmetry ($x \mapsto -x$, $\Delta T \mapsto -\Delta T$) does not hold anymore in cylindrical coordinates. Observations in cylindrical geometry with exchanged hot and cold sides [13] are then different and will be reported elsewhere.

Let us recall observations in rectangular geometry [11, 12] with large aspect ratio. In this experiment, a transition was reported from a line-source emitting planar waves at larger depth to a point source emitting locally cylindrical waves at smaller depth. This point source recalls the target pattern of HW2: the transition occurring at $h \simeq h_{\rm c}$ may be interpreted as the HW1/HW2 transition. A frequency shift was also measured at the transition. In both experiments, we observe a transition depth $h_{\rm c} \sim \lambda$ where $\lambda = \sqrt{(\sigma/\rho g)} = 1.4$ mm is the capillary length. The value of $h_{\rm c}$ may depend slightly upon the aspect ratios.

So the hydrodynamic behavior can be seen to change with the fluid depth h. This change may be explained by two different mechanisms:

- (i) the possible effect of the absolute fluid depth; this is accounted by the ratio $h/\lambda_{\rm c}$.
- (ii) the possible effect of confinement, inhibiting the spatial structure in the small horizontal dimension [11, 12]. This is related to the horizontal aspect ratio Γ_r.

Mechanism (i) suggests that if the depth h is lower then capillary length, the instability will be linked with

capillary effects. Qualitative observations allow us to suggest that HW2 are connected with surface deformations. On the other hand, mechanism (ii) relies only on aspect ratio and geometrical effects; the reduction of Γ_r will tend to transform a bidimensional system into an unidimensional one, and so HW2 into HW1. Of course, if one keeps the same experimental cell – as we do in this paper – the two mechanisms are linked and it is impossible to separate them. To discern between those two interpretations, one should build two apparatus with the same aspect ratio, but different absolute fluid depth; another way to determine the right mechanism would be to operate with fluids of different surface tension, *i.e.*, different λ_c, and to verify the conjecture $h_c \simeq \lambda_c$. While this work remains to be done, the hypothesis (ii) seems to us to be the most relevant.

Some critical behaviors of the HW2 pattern have been isolated. The amplitude and the width of the main peak in the power density spectra both evolve as $(\Delta T - \Delta T_{HW2})^{1/2}$. The amplitude behavior is a classical result for a pattern coming out of a supercritical instability. The broadening of the spectrum allows one to define it as another order parameter. It measures the apparitions of defects such as sources and sinks of waves in the pattern. An explanation for its smooth variations with ΔT cannot be found easily but may be linked to the large number of degrees of freedom excited in an extended geometry and the rapid decrease of the coherence length. As far as we know, no such behavior was reported so clearly neither in extended 1D-geometries, nor in 2D. The continuous transformation of HW2 from targets to opening spirals is measured by the variation of the azimuthal wavenumber with a critical behavior in $(\Delta T - \Delta T_{HW2})$.

The HW2 instability is localized, but this is not due to a localization of the temperature gradient in the corresponding spatial domain, as proved by a radial temperature measurement.

This work suggests different further investigations. We expect the thresholds $\Delta T_{HW1,2}$ of the instabilities to cross for intermediate value of the layer depth $1.2 < h < 1.9$ mm, *i.e.*, we can expect to face a codimension 2 point, and then study the competition of the two waves near onset. The transition to spatio-temporal chaos, obtained here for $h = 1.2$ mm with HW2 between 7.5 and 18 K has revealed power law spectra that should be analyzed in details. In particular, a very small increase of ΔT (to reach twice the threshold value) drives the system in a phase chaos state, while the corresponding Marangoni numbers are only twice the critical value. This hydrothermal waves system allows us to study the effect of the second horizontal dimension on a supercritical wave pattern, a very rich non-linear system far from being well understood yet.

We thank C. Gasquet who developed the image and signal acquisition software, V. Padilla and G. Francinet for technical support on the construction of the apparatus.

References

1. H.C. Kuhlmann, *Thermocapillary convection in models of crystal growth* (Springer Verlag, Berlin, 1999).
2. M.K. Smith, S.H. Davis, J. Fluid Mech. **132**, 119 (1983).
3. F. Daviaud, J.M. Vince, Phys. Rev. E **48**, 4432 (1993).
4. D. Villers, J.K. Platten, J. Fluid Mech. **234**, 487 (1992).
5. R.J. Riley, G.P. Neitzel, J. Fluid Mech. **359**, 143 (1998).
6. M.A. Pelacho, J. Burguete, Phys. Rev. E **59**, 835 (1999); M.A. Pelacho, A. Garcimartin, J. Burguete, Phys. Rev. E **62**, 477 (2000).
7. J.-F. Mercier, C. Normand, Phys. Fluids **8**, 1433 (1996).
8. J. Priede, G. Gerbeth, Phys. Rev. E **56**, 4187 (1997).
9. J.-F. Mercier, C. Normand, submitted to Int. J. Heat Mass Transfer (1999).
10. N. Mukolobwiez, A. Chiffaudel, F. Daviaud, Phys. Rev. Lett. **80**, 4661 (1998).
11. N. Garnier, A. Chiffaudel, F. Daviaud, in *Comptes rendus de la 2^e rencontre du non-linéaire*, edited by Y. Pomeau, R. Ribotta (Editions Paris Onze, 1999), p. 193.
12. J. Burguete, N. Mukolobwiez, F. Daviaud, N. Garnier, A. Chiffaudel, *Buoyant-thermocapillary instabilities in an extended liquid layer subjected to a horizontal temperature gradient*, submitted to Phys. Fluids (2000).
13. D. Shwabe, U. Möller, J. Schneider, A. Scharmann, Phys. Fluids A **4**, 2368 (1992).
14. B. Janiaud, H. Kokubo, M. Sano, Phys. Rev. E **47**, R2237 (1993).
15. D.R. Vrane, M.K. Smith, *The influence of domain curvature on the stability of viscously-dominated thermocapillary flows*, in *Advances in multi-fluid flows*, *AMS-IMS-SIAM Joint Summer Research Conference, 1996*, edited by Y. Renardy, A. Coward, D. Papageorgiore, S.-M. Sun,
16. M.C. Cross, P.C. Hohenberg, Rev. Modern Phys. **65**, Part II, 851 (1993).